Mechanistic understanding of microstructure evolution in extrusion-based additive manufacturing of stainless steel using modeling, simulation, and experimental analysis

Dayue Jiang [a,b], Yue Zhou [c], Mark D. Poliks [a], Peter Borgesen [a], Fuda Ning [a,*]

[a] Department of Systems Science and Industrial Engineering, State University of New York at Binghamton, Binghamton, NY 13902, USA
[b] Department of Industrial and Manufacturing Engineering, California State Polytechnic University Pomona, Pomona, CA 91768, USA
[c] Department of Aerospace Engineering, Embry-Riddle Aeronautical University, Daytona Beach, FL 32114, USA

A B S T R A C T

Extrusion-based additive manufacturing (AM) has been widely adopted as a cost-effective approach to building metal materials for engineering applications. The final microstructure and properties are strongly dependent on the post-processing, e.g., debinding and sintering, of the as-printed part. In this study, the structure evolution at a microscopic length scale during this extrusion-based AM process was understood by discrete element modeling, simulation, and experimental validation. In the simulation three groups of stainless-steel particles were placed with different distribution patterns by imposing different packing strategies. By considering both surface and grain boundary diffusion mechanisms during modeling and simulation, the microstructural evolution, including pore size reduction and grain growth were revealed. Effects of particle distribution patterns on the grain and pore morphology during sintering have also been uncovered. The simulation results were experimentally validated by characterizing stainless steel specimens at different sintering stages through X-ray computed tomography and microscopies, indicating their good alignment with the realistic microstructure evolution. The research findings from this study provide valuable insights into unique sintering behaviors affected by AM and guide the process optimization for metal alloys fabricated through the extrusion-based sintering-assisted AM process.

1. Introduction

Additive manufacturing (AM) has become an attractive alternative to traditional manufacturing technologies for metal component fabrication due to its advantage in rapid, freeform prototyping. Among all existing AM techniques for building metal components, the extrusion-based sintering-assisted method offers high manufacturing efficiency, low cost, and low material waste, thus showing great promise for building large-scale components in various industries [1]. Such a multi-step manufacturing process starts with the additive creation of polymer-based, metal particle-filled "green" parts by fused filament fabrication (FFF), which is a process to extrude filament materials through a hotted nozzle and form the 3D shape onto the building platform. Then, a debinding process is applied to remove the polymeric binders in the "green" parts. After that, the debound part undergoes a high-temperature sintering process to burn out the residual polymers and coalesce particles to achieve the final dense component. The finished

part can reach a relative density of >0.95 and exhibit a strength similar to that of wrought metals and structures built by laser-based AM [2]. Compared with the laser-based AM, such an extrusion-based sintering assisted (ES)-AM pathway also favors scalable manufacturing and facilitates the fabrication of alloys with high laser reflectivity (e.g., copper and aluminum) and high melting point (e.g., tungsten) [3,4].

The structural and mechanical properties of the ES-AM-built metal components have been widely studied mostly through experimental observations. Thompson et al. and Liu et al. found that pores were distributed along the boundaries of equiaxed grains in the 316 L stainless steel part built by ES-AM [2,4]. Kurose et al. found an anisotropic pore distribution induced by varying layering directions [5]. They also tested the tensile properties in different directions and found that the highest strength was obtained from the transverse direction. Pellegrini et al. [6] studied the effects of printing orientation on the resultant shrinkage and geometric accuracy and a strong shrinkage anisotropy has been found. Recently, Li et al., provided a study in comprehensive optimizing each

step of the ES-AM process to build steels with low porosity, high tensile strength and elongation [7]. Such experimental observations qualitatively reflect the significant role of printing and sintering processes in determining the anisotropic microstructures and resultant properties, yet exhibit limitations in discovering the underlying mechanisms that govern the sintering behaviors. To establish a quantitative correlation between process parameters and resultant microstructures, a physics-informed computational approach should be leveraged to simulate and explain the phenomena of microstructure evolution during the ES-AM process.

At present, a mechanistic understanding of microstructure evolution during the extrusion-based sintering-assisted AM process is not available. However, the sintering process has been well studied that build physics-driven models to understand the microstructure evolution phenomena. At the atomic scale, molecular dynamics (MD) simulations effectively predict the thermodynamics behind the particle coalescence and elemental diffusion during the sintering [8,9]. The MD method addresses nanoparticles to understand the atomic diffusion behavior; however, it doesn't allow to directly simulate micro-scale phenomena, such as pore evolution and grain growth. At the micro-scale, sintering leads to particle coalescence driven by the mass transfer at their boundaries/necks [10]. Based on the coalescence behavior, computational modeling has been developed to unveil the temperature-dependent evolution of microstructures including pores, grains, and local defects in the parts built by metal injection molding (MIM). Currently, approaches of micro-scale numerical simulation of sintering include Monte Carlo (MC) [11–13], phase field [14,15], and discrete element methods (DEM) [16]. Due to the limitation in computational cost from the sintering physics and model complexity, MC and phase-field approaches could only solve small-packing problems within hundreds of particles [17], unable to represent a more realistic dimension scale. DEM models can solve the problem of large particle assembly efficiently by avoiding the constraints in other methods, e.g., the mean-field strain assumption, thus reducing the computational cost. In the DEM, a large number of particles (usually in several tens of thousands) can be randomly distributed in a prescribed simulation box, and then the number of contact boundaries between particles is determined [18]. The contact law between particles is pre-defined in the model based on several contact evolution mechanisms. After calculation, the displacement of each particle is computed by Newton's second law of motion with their position updated till the simulation termination at a given criterion (e.g., time, volumetric strain, or relative density of the system).

The DEM model for the prediction of microstructure during sintering has been significantly developed from its initial form as introduced by Parhami and McMeeking [19]. In their model, the contact force between two spherical particles of the same size was established considering the grain boundary diffusion as the major mechanism to drive the coalescence. The determination of the contact size was achieved by Coble's contact radius evolution eq. [20]. Pan et al. [21] improved the expression of contact force between two particles of different sizes. With initial DEM models, critical phenomena during sintering have been studied in the past few years, such as particle rearrangement behavior [22,23], multi-material densification [24], microstructural evolution with constrained sintering on a substrate [25], etc. It was also found that the evolution of small defects and pores during sintering could be accumulated from local density heterogeneity, which may also be mitigated by particle rearrangement [26]. Recently, a grain growth model has been implemented into the DEM model to fully incorporate mass transport between particles [27]. The simulation predicted grain size growth in the sintering of alumina under different initial particle size distributions. Anisotropic sintering simulation was also performed with assembled particle chains (pre-aligned particles) [28], showing the number of aligned contacts affected the anisotropic shrinkage of the component. All those research findings have demonstrated the use of DEM to simulate a realistic sintering process, yet they have not incorporated large packing of particles with anisotropic pore distribution,

which is a particularly unique character induced by AM, into the DEM modeling. Therefore, to predict and understand the anisotropic microstructure evolution during sintering induced by extrusion-based AM, there is a growing need to develop a more precise and robust DEM model.

In this study, the fundamental understanding of microstructure evolution of stainless steel built by ES-AM will be established by leveraging a physics-driven DEM model that accounts for the role of distribution patterns of large particle packing. The objective of this study is to understand the microscale relationship between the extrusion-based sintering-assisted process and the associated microstructure evolution. The pore evolution and grain growth phenomena will be predicted from the initial packing state to the final sintered state and validated by experimental characterizations. The completion of this study will fill the knowledge gap in microscale understanding of sintering during ES-AM, and advance the design, fabrication, and application of ES-AM-built metals with predictable microstructures.

2. Modeling process

2.1. Model description

The discrete element method (DEM) is a physics-informed, computational approach to simulate the interaction between particles based on Newton's second law of motion. It has been utilized to predict microstructural evolution during the solid-state sintering process. Fig. 1 demonstrates the overall framework of the DEM simulation for the whole sintering process. An initial group of particles is generated with assigned size distribution in the first step. Three-dimensional coordinates and the radius of each particle are stored in the initial coordinate file. Next, the contact law is defined on any particle that connects neighboring particles, and their relative displacements are calculated. Meanwhile, grain coarsening law is implemented based on surface and grain boundary migration mechanisms to compute the size evolution. An updated coordinate file is then produced to input into the second step. During simulation, coordinate files are exported with a relative density (RD) increment of 0.01. The simulation will terminate at a critical RD of 0.90, which represents a high densification status in the final part.

Particles, as the fundamental element in the DEM, possess single crystallographic grain and will be packed together inside a simulation box. In nature, particles can be either single-crystal or polycrystalline, but the DEM method is not able to capture the atomic-level interactions within a particle. Each particle is regarded as a perfect sphere and labeled with a position in *x*, *y*, and *z* coordinates and its radius. Some other important assumptions in the DEM model include:

(1) Before sintering, particles are densified from a state of zero contact (RD = 0.3) to a compact state with several elastic contacts (RD = 0.51) in order to reach a comparable volume fraction of particles in the pre-sintered state. Those contacts evolved based on the Hertzian contact model [29].

(2) No rotational forces will be imposed on the particles. The effects of binders are not considered.

(3) Two major diffusion mechanisms, namely surface diffusion and grain boundary diffusion, are considered the driving phenomena of sintering [27]. Their diffusion coefficients are both temperature-dependent, following the Arrhenius form. The particle evolution/grain growth is governed by the surface diffusion and grain boundary migration in which mass transfer occurs across the grain boundaries.

(4) There will be a heating and holding period during the sintering simulation. The heating starts at 1050 °C with a ramping rate of 5 °C/min until 1350 °C. No cooling stage will be imposed.

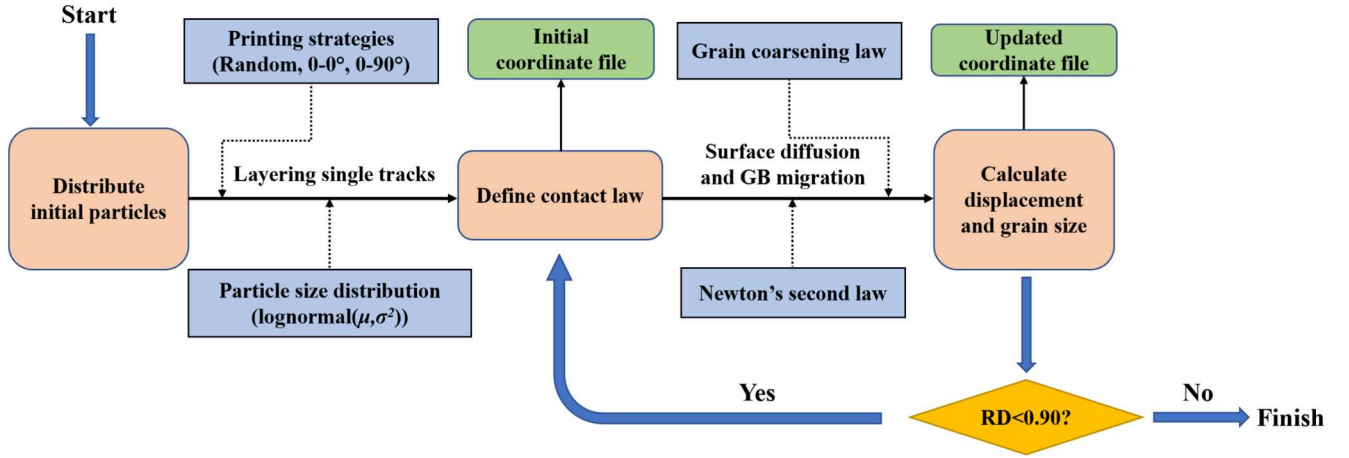(5) Other than predefined pore distribution in the part, the manufacturing defects caused by FFF (e.g., impurities,

Fig. 1. Framework of DEM simulation.

deformation and warping, inconsistency of density) will not be reflected in the geometry. Gravity will also be neglected.

2.2. Particle assignment under printing strategies

The printing path creates initial anisotropy inside the pre-sintered part and impacts the mechanical property of the final sintered component [30]. To mimic the anisotropic particle distribution, we designed three strategies of particle packing in the binder-free pre-sintered part status, as illustrated in Fig. 2. In a random particle distribution pattern, 12,500 particles without contact were first placed inside a cubic simulation box (size ratio equals to 1:1:1) with a relative density of 0.30. The size of particles followed a lognormal distribution with an average diameter of 5.5 μm and a standard deviation of 0.3 μm [31]. To numerically "stack" particles together, the "jamming" process was utilized to initially compress the loose particles (zero contacts) to a relative

Fig. 2. Packing strategies of particles for the DEM modeling. (a) *Random* pattern, (b) *0–0°* pattern, (c) *0–90°* pattern, and (d) 12,500 particles packed under a *0–0°* pattern.

density of 0.51 (jammed state described in Appendix A). The cubic simulation box has a side length of 0.15 mm (Fig. 2(a)). Meanwhile, we created another two patterns, including the *0°-0°* pattern and *0°-90°* pattern, as shown in Fig. 2(b) and (c), respectively. In both patterns, we assume that a single track of the as-printed part will contain 500 particles, and in a x, y, z ratio of 1:5:1. To create the total 12,500 particles with desired distribution, five "jammed" tracks were parallelly created that present the part printed in a single layer. Finally, such procedure was repeated in creating a total of 5 layers. We found that a total of 12,500 particles can provide enough information on the large-scale microstructure including the pore distribution and grain evolution without using considerable computational time. The *0–0°* pattern was created by depositing five identical layers along the same direction, whereas the *0°-90°* pattern altered the interlayer angle by 90°. Within each track, the size of particles followed the same size distribution. Fig. 2 (d) shows the cubic simulation box containing a total of 12,500 particles in a *0–0°* pattern.
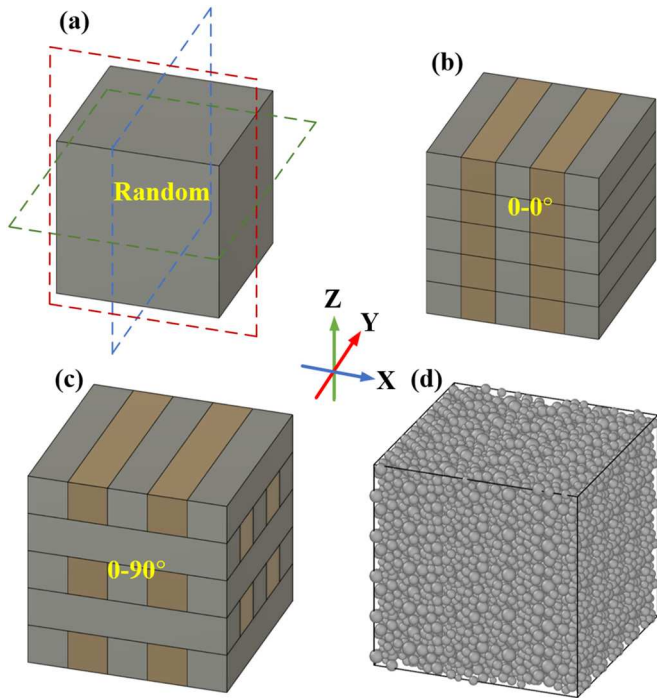
2.3. Contact law and grain growth models

After the initial generation of particles, the simulation was performed using an open-source DEM code, dp3D, developed by the SIMaP laboratory in France [16]. This code has been successfully utilized to simulate different physical phenomena and rigorously improved by researchers for higher accuracy and more applicable fields in the past decades [32–35]. As shown in Fig. 3, two particles with sizes r_s and r_l have an indentation thickness of h. During sintering, a Bouvard-Pan contact law between particles is defined [27]:

$$N_S = -\frac{\pi a^4}{\left(1+\frac{r_s}{r_l}\right)\beta\Delta_{GB}}\frac{dh}{dt} + \frac{\alpha}{\beta}\pi r_l\gamma_s$$

$$\Delta_{GB} = \frac{\Omega}{k_b T}D_{GB}\delta_{GB}$$

$$(1)$$

where N_S is the contact normal force, a is the contact radius, r_s and r_l are the radii for small and large particles, respectively. α, β, and Δ_{GB} are the diffusion-related terms, dh/dt is the neck width increment with time, and γ_s is the surface energy. Ω stands for the atomic volume and k_b is the Boltzmann constant. $D_{GB}\delta_{GB}$ is the term of grain boundary diffusion that follows an Arrhenius form. D stands for diffusion coefficient and δ_{GB} is the thickness of the grain boundary. The displacement of particles is derived based on Newton's second law of motion using a Velocity-Verlet algorithm.

Once the contact size between two particles achieves a critical value that is determined by the equilibrium dihedral contact angle, Ψ_{eq}, two grain-growth models will be imposed into Eqs. (2) and (3), respectively
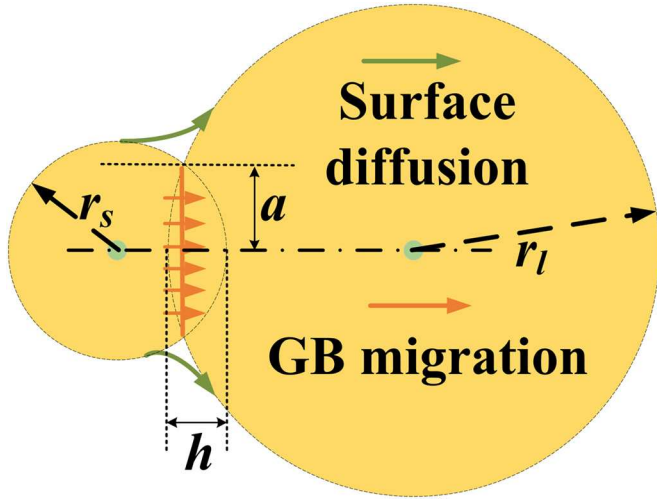
Fig. 3. Schematic of geometrical parameters for the Bouvard Pan contact law between a small and a large particle with radius r_s and r_l, respectively, and the illustration of sintering mechanism including surface diffusion at the edge of particles, and the grain boundary (GB) migration at the particle neck.

[27,29].

$$\left(\frac{dV_{l,s}}{dt}\right)_s = -2\frac{D_s}{k_b T}\gamma_s\Omega\frac{\frac{1}{r_l}-\frac{1}{r_s}}{r_l+r_s-h}\left[\pi(a+\delta_S)^2 - \pi a^2\right] \quad (2)$$

$$\left(\frac{dV_{l,s}}{dt}\right)_{GBM} = -2M_{GB}\gamma_{GB}\left(\frac{1}{r_l}-\frac{1}{r_s}\right)\left[\pi a^{*2}\right] \quad (3)$$

where $dV_{l,s}/dt$ is the mass flux during grain growth and M_{GB} is the temperature-dependent grain boundary migration coefficient also following the Arrhenius law. The contact neck size is assumed to be a constant, a^*, after the initiation of grain growth. Two fundamental mechanisms including surface diffusion and grain boundary migration contribute to the grain growth, resulting in the average size increase during the simulation. During surface diffusion, atoms move through the boundary of neck with a radius of a and thickness of δ_S, while for grain migration the diffusion area is the entire circle of the neck. The parameters retrieved from literature for the simulation are listed in Table 1.

2.4. Outputs of the DEM model

The sintering simulation was terminated at the relative density of 0.90. Table 1 lists the parameters for the DEM simulation of the 17–4 PH SS powders in this study. After simulation, a 2D image generator integrated in the dp3D was utilized to generate an image sequence containing both particles and their interfacial connections along the axial direction (cross-section plane in normal z). A total of 1000 slices were generated and exported as .raw file, which would be subsequently analyzed with ImageJ software. To obtain the information of localized porosity and the dimension of pores, each slice has been segmented to provide an areal information of the pores and the grain size. The average porosity for one slice was measured by dividing the area of pores to the total area of the figure, and the total pore area/grain size divided by the

number of pores/grains were treated as the average pore size and grain size for one slice, respectively. Such measurement procedure was repeated for all slices and the results were again averaged to summarize the entire information of the 3D pore size, porosity, and grain size. As the grain or pore shape is usually irregular which makes it difficult to quantify their size, here we assumed round circles to represent the same area, so the diameter of the circle is considered as the grain or pore size. On the other hand, the 2D raw data was also imported to an imaging process software, Dragonfly by Object Research Systems (ORS, Canada), for the 3D reconstruction of the 2D slices. Grains and pores were appropriately segmented to reveal the evolution of microstructure during the sintering process.

3. Experimental methods

3.1. Sample preparation

A 17–4 PH SS metal-polymer composite filament (17–4 PH, Markforged Inc., USA) was used as the feedstock for the FFF printing by a high-temperature desktop printer (Funmat HT, INTAMSYS Corp., China). The polymer binders in the filament include 20 vol% of wax and 20 vol% of polyethylene. The green specimen size was 5 × 5 × 1 mm. Similar to the simulation process, three different printing patterns were generated, including the *Random* pattern, a *0°-0°* pattern and a *0°-90°* pattern. The *Random* green specimen was created by first heating the debris of filament at 180 °C for 3 h, then hot pressed in a ϕ 8 × 4 cylinder container. The printing parameters for the other groups are listed in Table 2. After printing, samples were placed inside the debinding chamber (Wash-1, Markforged Inc., USA) to remove the wax binder in the green part. The duration of debinding was around 24 h in an Opteon SF79 solution (TMC Industries Inc., USA) at ambient temperature. A high-temperature furnace (Sinter-2, Markforged Inc., USA) was then utilized to sinter the part after solvent debinding under the protection of the mixture gas of argon and hydrogen. Specimens were taken out from the furnace during and after the sintering. Relative density of the specimens was tested via a gas pycnometer (Ultrapyc 1200e, Quantachrome, USA). Intermediately sintered specimens possessed a relative density of 0.83–0.86 and the specimens after full sintering had a relative density of 0.98.

3.2. Characterization of micropores and grains

The results from DEM simulation were compared with the experimental data. X-ray CT (Nanome X, Baker Hughes, USA) was conducted to measure the internal pore evolution of the specimen during sintering. Specimens at the intermediate sintering stage and the as-sintered stage were chosen for the X-ray CT scanning. The scanning voxel size was 10 μm while 1000 slices were reached along the longest direction. The 3D internal features were characterized by Dragonfly with the capability of quantifying the porosity of each slice from different orientations. Grain morphology was observed by an optical microscope (DSX 500, Olympus, Japan) using the same specimens that were prepared by standard metallography procedures, and chemically etched by Marble's reagent. Grain sizes were measured on at least five images for a single specimen according to ISO 643 standard [40].

Table 1
Parameters used in the DEM simulation of 17–4 PH stainless steel.

$D_{0GB}\delta_{GB}$ (m^3/s)	5.4×10^{-14} [36]	Q_{GB} (kJ/mol)	155 [36]
D_{0S} (m^2/s)	372.4 [37]	Q_S (kJ/mol)	163.9 [37]
M_{0GB} $(m^3/(N \cdot s))$	2.03×10^{-4} [38]	Q_{GBM} (kJ/mol)	350 [38]
Ψ_{eq} (°)	138 [27]	Ω (m^3)	1.18×10^{-29}
γ_S (J/m²)	0.4 [39]	γ_{GB} (J/m²)	$2\gamma_S cos(\Psi_{eq}/2)$

Table 2
Printing parameters for the fabrication of green parts.

| Parameters	Values
Nozzle temperature	260 °C
Nozzle diameter	0.4 mm
Infill percentage	100%
Printing speed	30 mm/s
Layer height	0.1 mm
Bed temperature	90 °C
Chamber temperature	70 °C

4. Results and discussion

4.1. Sintering kinetics

Fig. 4 exhibits the side view of particles/pores in a pre-sintered state and the curves retrieved from the simulation that describe some essential attributes of sintering kinetics, including densification, densification rate, and grain coarsening. Unlike a random distribution of pores shown in Fig. 4(a), interlayer gaps are indicated in the *0–0°* and *0–90°* particle packing patterns. Those interfacial gaps are typical features observed in parts built by the FFF process [41]. As the temperature ramps up, the RD values gradually increase with the sintering time, as indicated in Fig. 4 (d). The densification rate then apparently slows down during the

holding stage above an RD value of 0.8 to the final RD of 0.9. The *Random* group exhibits the highest densification rate as they reach the final RD faster than the other two, followed by the *0–0°* group. From the simulation, it would only take less than 3 h for the *Random* group to reach RD of 0.9 but >6 h for the 0–90 group, suggesting a major impact of initial particle/pore distribution on the densification behavior.

Fig. 4(e) shows more details about the densification rate with the progression of RD values. The *0–0°* and *Random* group exhibit similar densification rates at RD values below 0.8, both of which are slightly higher than that of the *0–90°* group. On the other hand, both *0–0°* and *0–90°* groups have a great reduction of densification rate at RD values above 0.8 while the *Random* group exhibit a smaller reduction of the densification rate. Fig. 4(f) depicts the grain coarsening behavior during
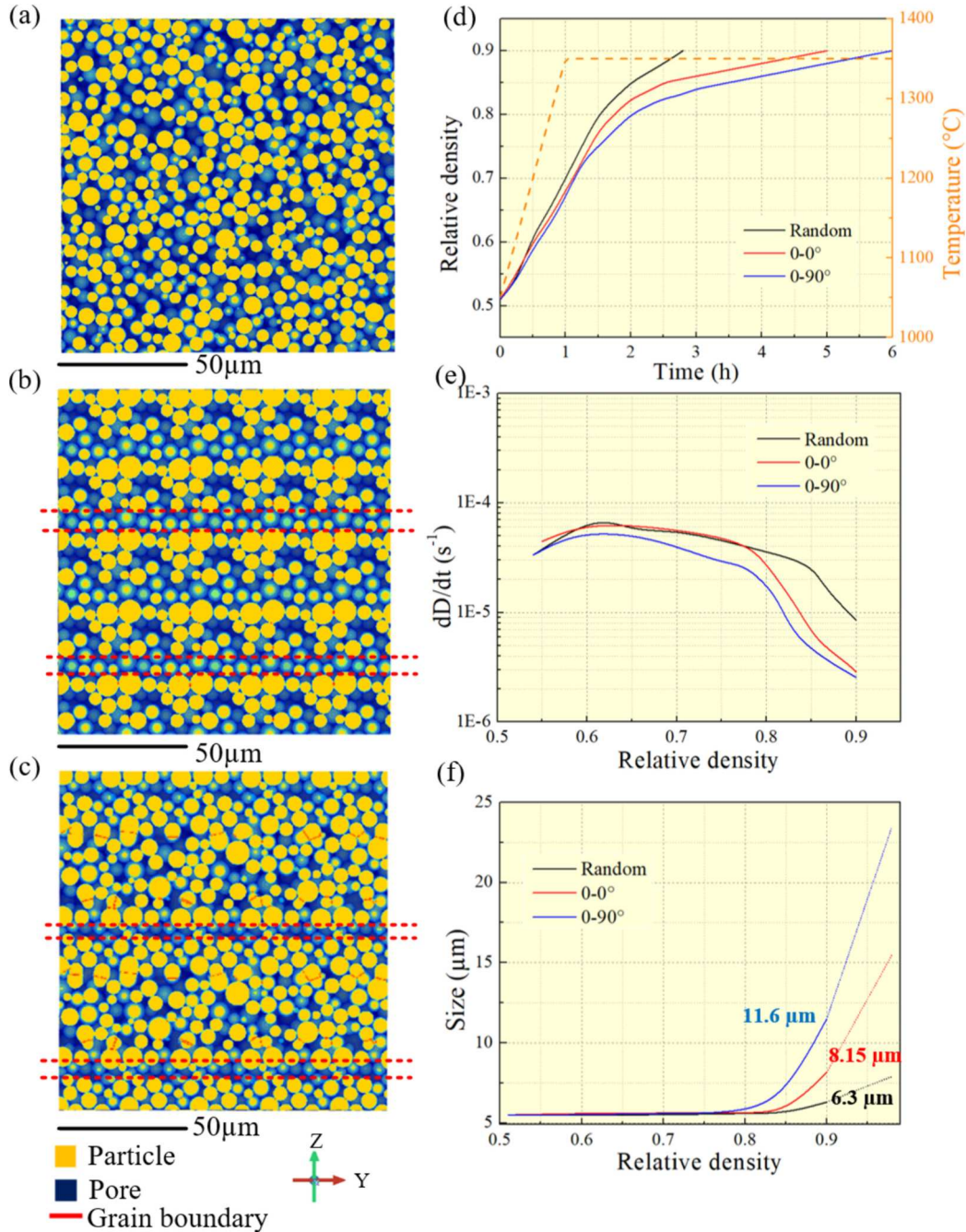
Fig. 4. Sintering behaviors of 17–4 PH SS for three different groups, including the side surface in (a) *Random* group, (b) 0–0° group, and (c) 0–90° group. Interfacial gaps are highlighted in (b) and (c) as a result of connected pores. (d) Densification curve versus time. (e) Densification rate at different densities. (f) Grain size evolution and the predicted final grain size at RD = 0.98.

sintering. Before the RD value of 0.8, limited grain growth is observed for all three groups. The 0–90 group experience the highest speed of grain coarsening compared to other groups when the RD value goes above 0.8. The grain size at an RD of 0.9 reaches 11.6 μm in the *0–90°* group, followed by 8.15 μm in *0–0°* group and 6.3 μm in the *Random* group.

The difference in densification behavior and grain coarsening rate indicates a significant impact of initial pore distribution. In the DEM simulation, interconnected particles experience different stages of coalescence driven by the diffusion mechanisms. At the beginning where the contact size is minimal, surface diffusion is dominant to facilitate the densification and form the neck, then the grain boundary diffusion becomes more effective with the neck growth. Such a transition is because the surface contact area shrinks when the connecting neck size becomes larger. Meanwhile, grain coarsening is enabled by the mass transfer from the surface diffusion and grain boundary migration. Reduced densification is usually accompanied by grain coarsening because a large neck size could generate great resistant force against further densification [42]. In this study, it can be seen that grain coarsening is rather dominated by the grain boundary migration since the grain size has merely increased for lower RD values below 0.8. Moreover, due to the formation of interlayer gaps, *0–0°* and *0–90°* groups exhibit greater grain coarsening than the *Random* group because particles are more concentrated between those gaps, creating more contacts and greater contact size growth, eventually resulting in a higher average grain size and smaller densification rate.

4.2. Grain growth behavior

The microstructural evolution during sintering is simulated for each
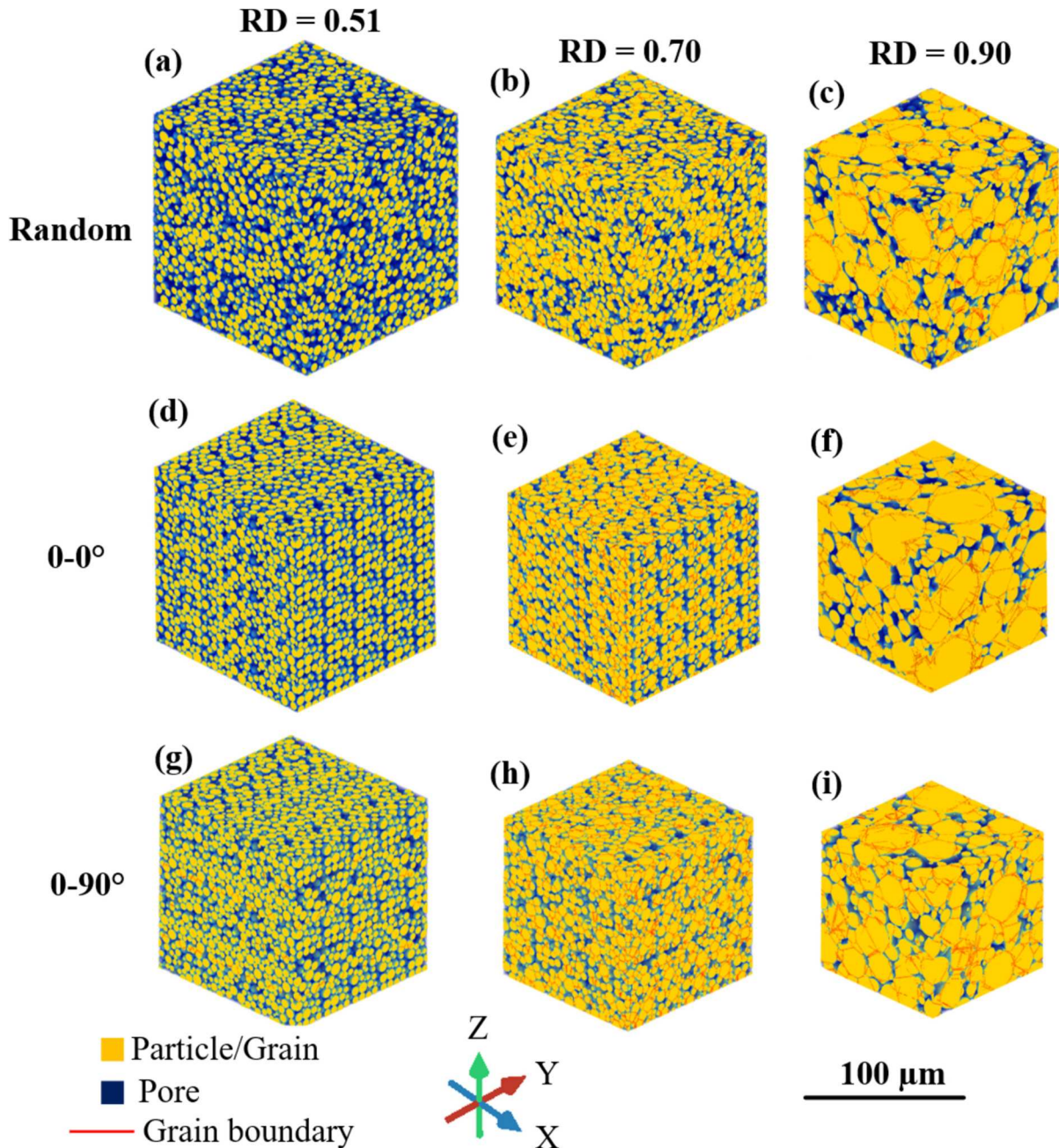
Fig. 5. Microstructure evolution of 17–4 PH SS during sintering including the initial stage (RD = 0.51), intermediate stage (RD = 0.70), and final stage (RD = 0.90) for three groups.

printing pattern from the initial stage (RD = 0.51) to the final stage (RD = 0.90), as shown in Fig. 5, where the yellow region represents the grains and the blue color depicts the pore area. A final RD of 0.9 was set to account for a more accurate final grain size prediction as the DEM model may not appropriately capture the polygonization of grains at the near net-dense stage [42]. The average grain size (*G*) can be calculated by an inverse square root law with the porosity (*θ*): $G = \frac{AG_0}{\sqrt{\theta}}$. *A* is fitted to be 0.64, 0.79, and 0.90 for *Random*, *0–0°*, and *0–90°* groups, respectively [43]. To compare with experimental results, we extend the simulated curve of grain size to an RD of 0.98, making their grain sizes become 23.4, 15.8, and 7.9, respectively. The predicted grain sizes are matchable with those reported by other researchers [44,45].

As shown in Fig. 4(f), the grain size increases with the RD and the growth rate would accelerate at a higher RD. Fig. 5 shows a coalescence of particles by forming connecting necks (red lines), which are then enlarged as the densification proceeds, and finally, neighboring grains are integrated in the form of grain coarsening. In Fig. 5(a), the initial particles are distributed randomly inside the simulation box. The distribution pattern of particles can be recognized for the *0–0°* group and *0–90°* group at RD of 0.51. Those patterns, induced by the periodic packing strategies, create local pore concentrations at intralayer and interlayer spaces.

Three groups exhibit similar grain growth rates at the initial and intermediate stages. At the RD of 0.7, the number of contacts increases significantly due to the overall densification, but the grain sizes are not greatly enlarged. As shown in Fig. 5(b), (e), and (h), most particles remain at the same location so that the pore distribution pattern can still be observed. Significant grain growth occurs in all three groups for RD values between 0.70 and 0.90. Fig. 4(f) suggests that the grain growth for the *Random* group is slower than for the other two. This phenomenon could be explained by the difference in grain-pore interactions.

Fig. 5(e) and (h) show that the phenomenon of pore concentration during initial packing still exists for these two groups in the intermediate sintering stage, promoting a greater grain growth rate. Specifically, after the intermediate stage, grain growth will be dependent on the solid-solid interface and the number of grain boundaries [46]. As a result, the concentration of pores dictates the number of grain boundaries inside the part. Thus, grain growth would be facilitated if the pores are more concentrated, corresponding to denser contacts of grains. In the cases of *0–0°* and *0–90°* printing patterns, both particles and pores are more concentrated due to the initial assignment of pores along the inter and intra-layers, contributing to a more significant grain growth than for the *Random* group. Comparing the *0–0°* and *0–90°* groups, the *0–90°* group is seen to exhibit a higher grain growth rate and a larger final grain size due to even higher pore concentration by the alternation of particle packing direction. The grain growth should be controlled during the sintering process as larger grains reduce the strength and ductility of the material. Therefore, a printing strategy with more randomness and prevention of pore connection would benefit the final performance of the sintered component.

The grain morphology from experimental observation at different sintering stages is shown in Fig. 6 and the corresponding grain sizes are quantified in Fig. 7. At the intermediate stage, the 17–4 PH SS is mainly comprised of martensitic structure. The average grain size for the *Random* group barely increases and is smaller than the other two groups. When further sintered, more austenitic phases are observed in equiaxed grain structures. Therefore, it is anticipated that the 17–4 PH particles during sintering would undergo a phase transformation step from the martensite to austenite, regardless of the printing strategies. On the other hand, their average grain size has increased, especially for groups of *0–0°* and *0–90°*. Large variations of grain size are also observed for those groups because there are several extremely large grains (>50 μm) found in those groups, resulted from the interactions between pores and
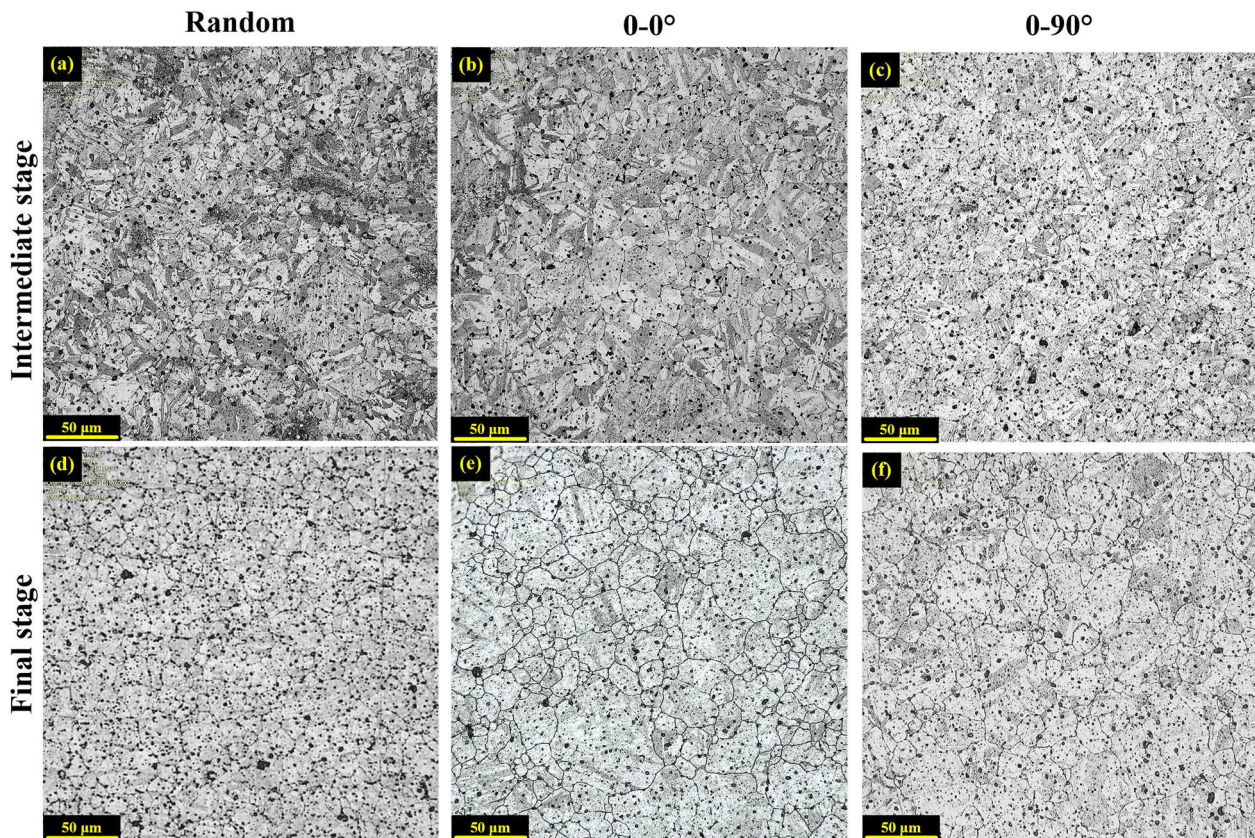

Fig. 6. Grain morphology of specimen at intermediate and final sintering stages for (a) and (b) *Random* group, (c) and (d) *0–0°* group, (e) and (f) *0–90°* group, respectively.
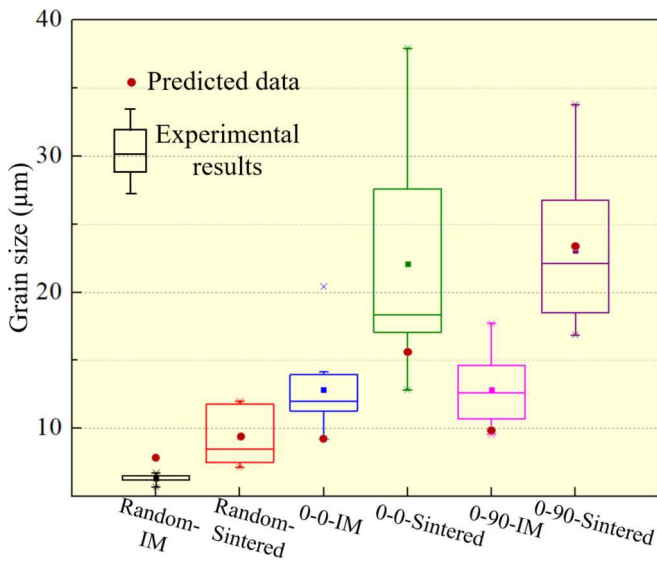
Fig. 7. Quantification of grain size at different sintering stages for three groups of specimens and comparison with the DEM prediction (IM: intermediate).

grains. The largest grain size is obtained from the *0–90°* group, which is consistent with the simulation result. Overall, the predicted value of the final grain size aligns well with the experimental results for grain morphology. Some variations could stem from the complex diffusion mechanisms during sintering and also the effects of phase transformation. The diffusion parameters given in the DEM model are constructed by simple Arrhenius-based equations that account for the temperature effect but neglect other phenomena like the formation of defects and phase transformation [47]. The DEM model can be further improved by considering those effects.

4.3. Pore evolution

The statistical distribution of local porosity simulated at the early stage of sintering (RD: 0.51) is shown in Fig. 8. The histograms for 2D slices of the *Random, 0–0°*, and *0–90°* groups along the building direction (XOY plane) are demonstrated respectively. The distribution pattern from the *Random* group is close to a normal distribution and porosity values mostly fall in the range between 48% and 54%. The distribution patterns become off the normal distribution for both *0–0°* group and *0–90°* group with a larger average porosity. For the *0–0°* group, two distribution peaks can be found at around 51% and 54%, indicating the pore concentration behavior. Such phenomenon is also found for the *0–90°* group, where the highest concentration of porosity is found to be 52% and 56%, showing a greater area of connected pores induced by additive manufacturing before sintering. After the completion of sintering, such a tilted porosity distribution for *0–0°* and *0–90°* groups still exists and a small portion of high porosity layers can be determined from the histogram. Similar to the pre-sintered stage, porosity values for the *Random* group exhibit a pattern close to normal distribution after sintering.

Difference in spatial porosity distribution at the early stage has resulted in very different pore sizes at the end of sintering. Fig. 9 exhibits the pore geometry and histograms of simulated pore sizes in later stages of sintering (RD = 0.9). Pore geometry is also exhibited in parts at RD = 0.7. For the *Random* group, small pieces of pores are distributed at the surface when RD = 0.7, and the number of pores on the surface reduces at RD = 0.9. However, one large, connected pore is visualized in the 3D model at RD = 0.9 shown in Fig. 9(c), which could be due to the pore coalescence (small pores connect with neighboring ones due to particle movement) at the intermediate and final stages of sintering [48]. For the other two groups, the pore distribution on the surface reflects the printing pattern at the intermediate state of sintering. At RD = 0.9, it has also been revealed that despite the reduction of porosity on the surface, pores are also connected inside the part. It should be noted that this pore geometry may not be representative of that at RD = 0.98 because the grain size can significantly increase for RDs from 0.9 to 0.98. As a result,
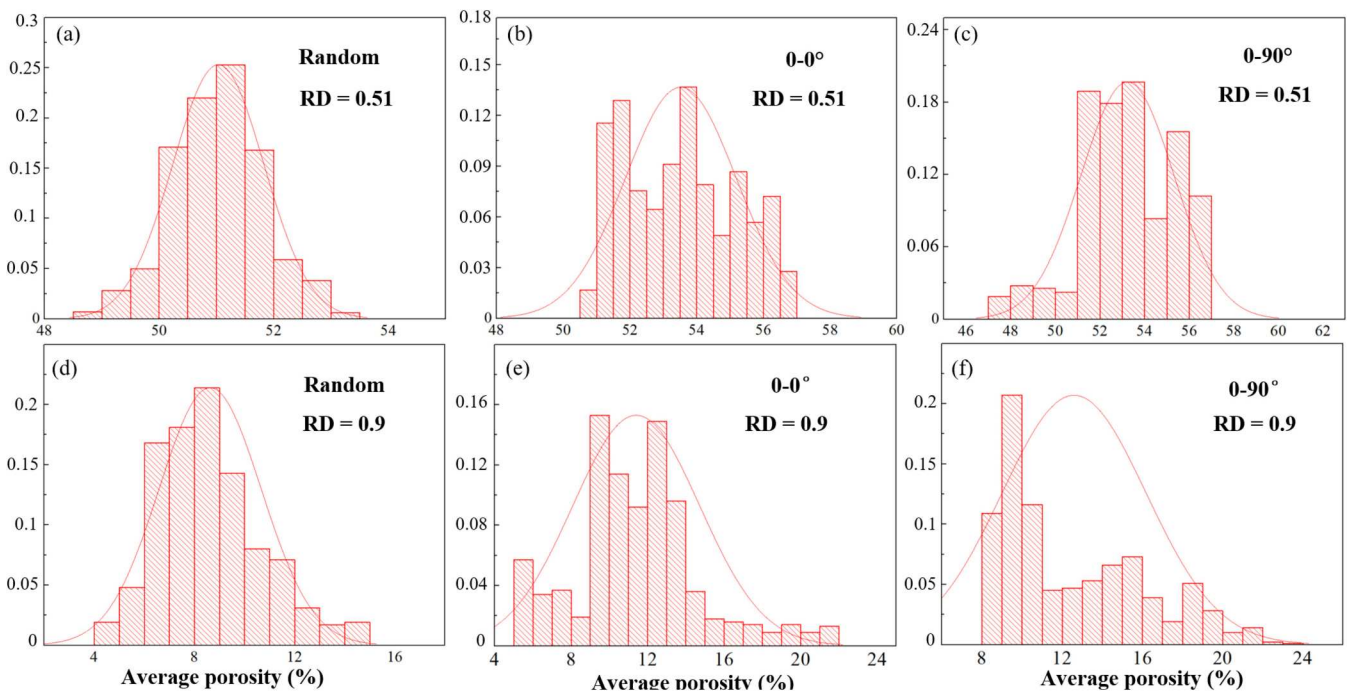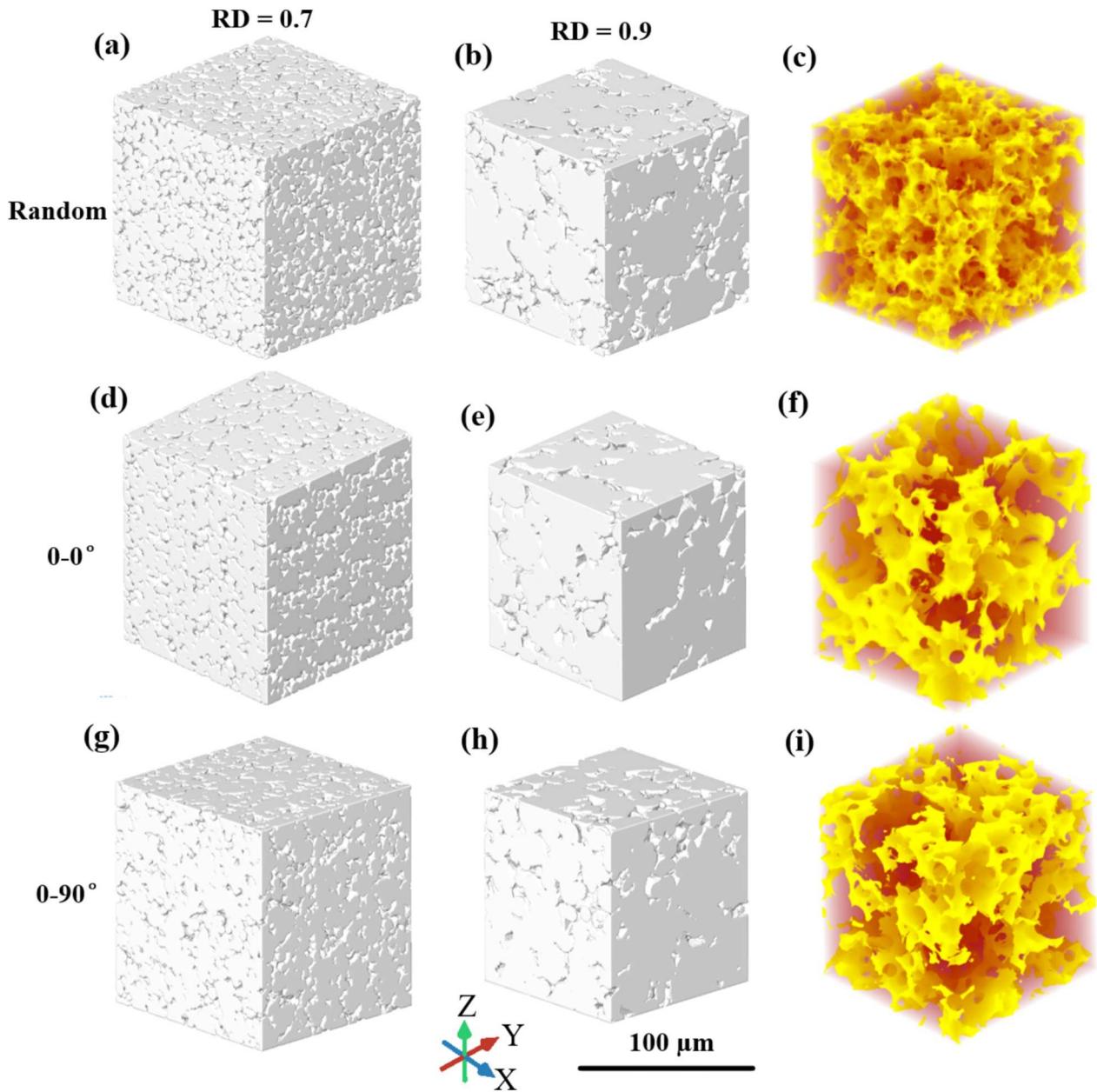

Fig. 8. The histograms of porosity distribution for (a, d) *Random* group, (b, e) *0–0°* group, and (c, f) *0–90°* group at relative densities of 0.51 and 0.9 for all groups, representing the initial stage and final stage of sintering, respectively. 1000 XOY slices were taken from the bottom to the top and the porosity was analyzed by imaging processing software ImageJ.

Fig. 9. Distribution of pores on three surfaces for all groups at relative densities of 0.7 and 0.9. (c), (f), and (i) display the 3D visualization of pores (in yellow color) inside the part (in red color) of the *Random* group, *0–0°*, and *0–90°* group of specimens at RD = 0.9, respectively. Pores are mostly connected at both sintering stages, so the pore size calculation was only conducted for the 2D slices. (For interpretation of the references to color in this figure legend, the reader is referred to the web version of this article.)

large, connected pores should be broken down to small pores. Additionally, the polygonization of grains also helps the enclosure of pores at the grain corners.

Due to the nature of DEM simulation that deals with spherical particles with no polygonization, pores are well connected that creates a single large volume (Fig. 9(c), (f), (i)), making it difficult to measure the pore size. The alternative is to measure a plane-wise porosity in slices along different directions, and the 2D porosity values are quantified along the *x*, *y*, and *z* axis, as depicted in Fig. 10. It is found that the porosity distribution is consistently random in the *Random* group at both RDs, and the average of porosity reduces from around 30 μm to 10 μm. Similar concentration of porosity is observed along every direction, suggesting the isotropic distribution. On the other hand, anisotropy is indicated for both the *0–0°* group and *0–90°* group. Specifically, the YOZ plane in *0–0°* group and XOY plane in *0–90°* group have the highest pore

concentration at the RD of 0.7, as indicated by their extremely high porosity values at several slices. This could reflect the interlayer gaps induced by the printing pattern. At RD = 0.9, porosity along those directions is reduced and its variation becomes matchable with other directions for both groups, showing the transition from anisotropy to isotropy in pore distribution under the progress of sintering.

4.4. Experimental validation of pore evolution

X-ray Computed Tomography (CT) scanning is conducted to experimentally characterize pores inside the specimens to validate the simulation results at different sintering stages. Fig. 11 exhibits the reconstructed geometries of cuboid specimens at (1) the intermediate (IM) sintering stage and (2) sintered stage. Pores inside the specimens are labeled by colors with respect to their volume. From Fig. 11(a) and
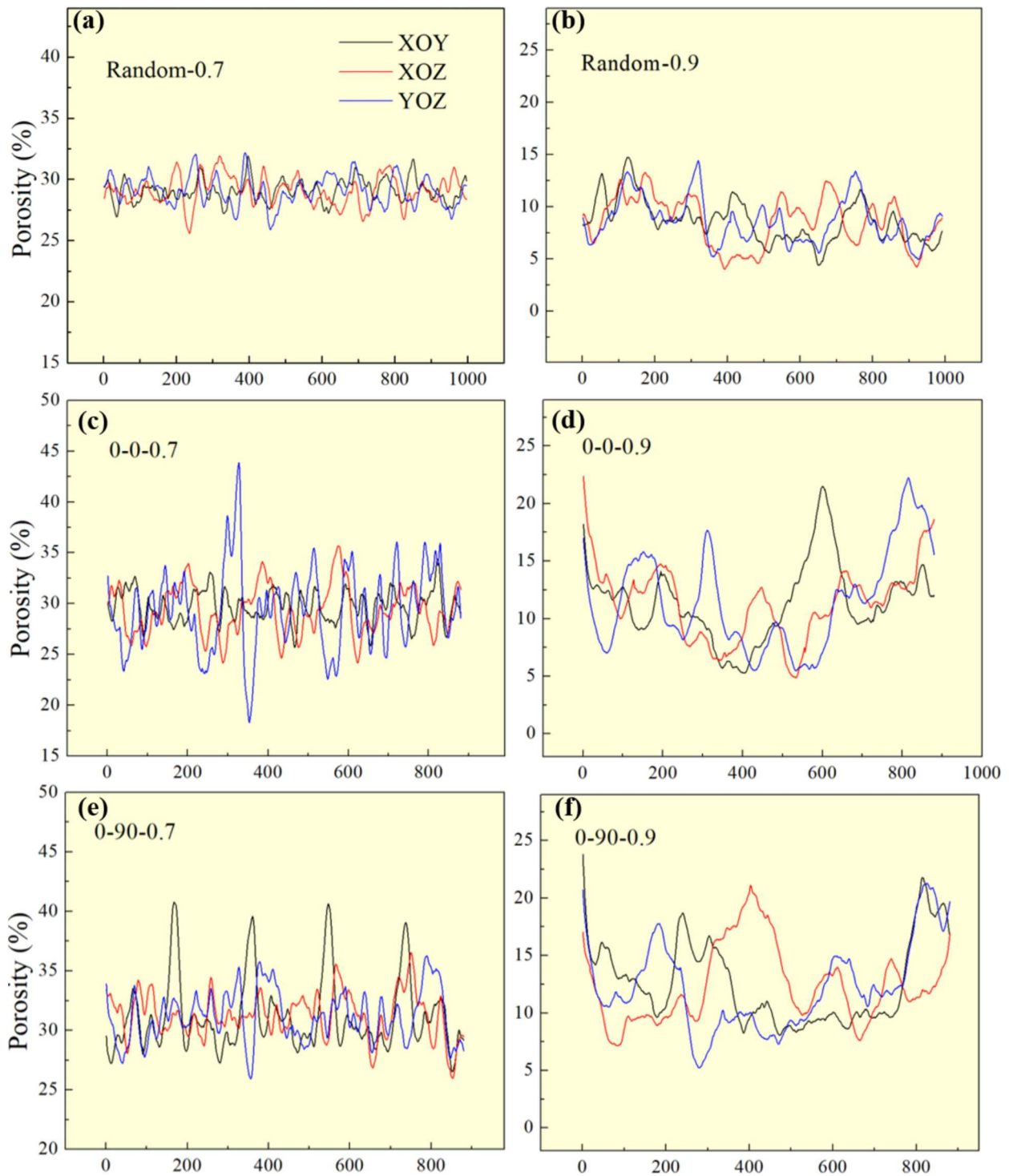
Fig. 10. Simulated plane-wise porosity distribution at two sintering stages for (a-b) *Random* group, (c-d) *0–0°* group, and (e-f) *0–90°* group of specimens with x, y, z representing normal directions to YOZ plane, XOZ plane, and XOY plane, respectively. Specimens are named by their group (*0–0°*, *0–90°* or *Random*) followed by the associated RD (0.7 or 0.9).

(b), pores are randomly distributed inside the sample from *Random* group, and both of their sizes and numbers have decreased in the sintered specimen. Unlike the *Random* group, pore distribution patterns can be identified in the *0–0°* and *0–90°* groups at intermediate stage. Several long pores (in red color) are observed for the *0–0°* group in Fig. 11(c) and (d) along the deposition direction within a layer. Those pores are an indication of intralayer gaps. The number of such pores is well reduced at higher RD, but the shape remains. In Fig. 11(e), the pore distribution reflects the 90° alternative printing pattern since most pores align parallelly in either x or y direction. Both the number and size of pores are significantly reduced in the sintered part shown in Fig. 11(f) whereas the distribution pattern of pores becomes random.

From the CT scanning, we can quantify the pore size inside the specimen at different sintering stages. Fig. 12 shows the histograms of the pore size distributions and the mean pore size for each group at different sintering stages. The smallest pores are obtained for the
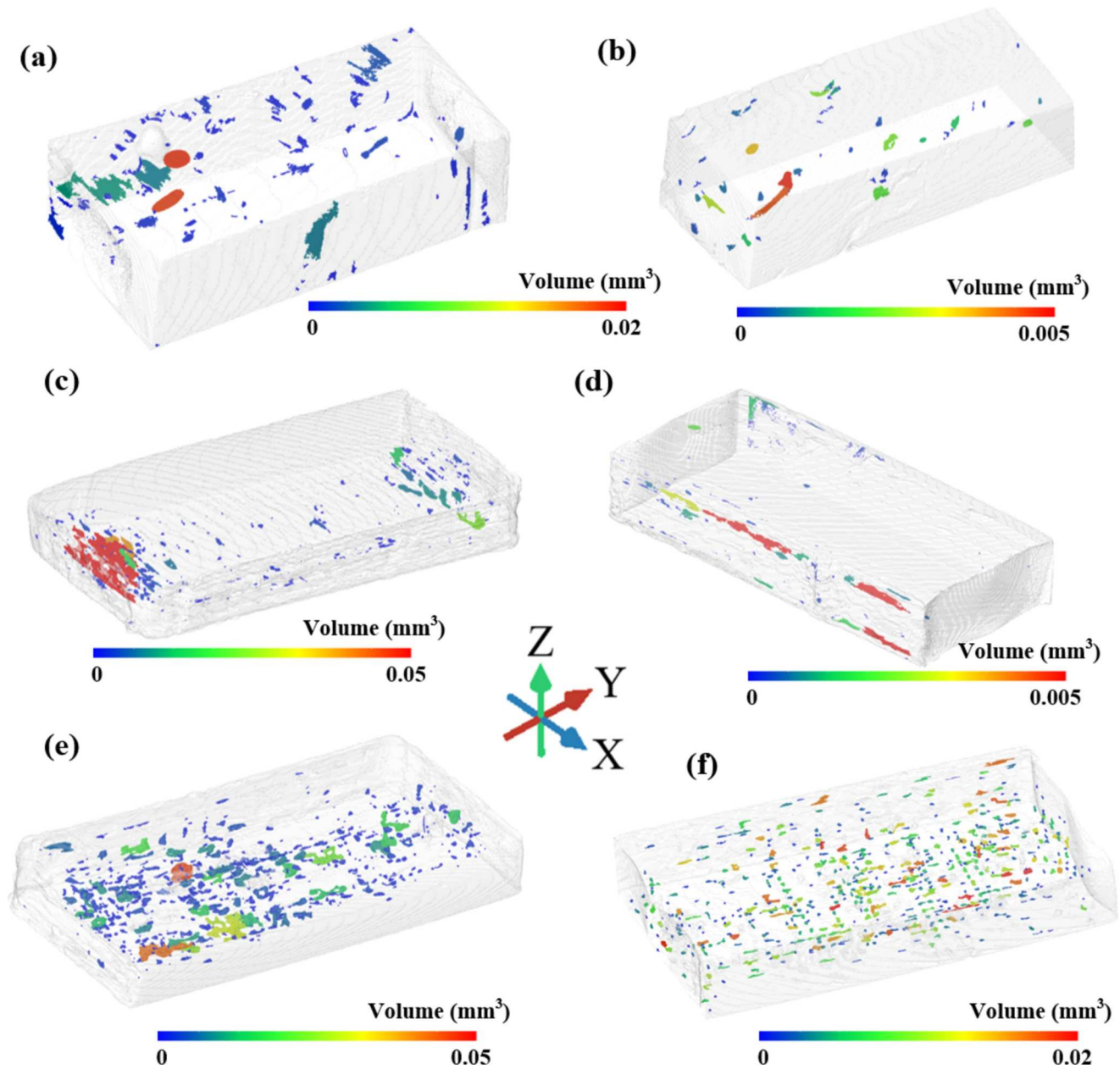
Fig. 11. 3D reconstructed geometry of specimens at intermediate and final sintered stages for (a-b) *Random* group, (c-d) *0–0°* group, and (e-f) *0–90°* group.

Random group, with 50% of the pores being <20 μm for both intermediate and sintered states. Although the number of pores is reduced in the sintered specimen, the average pore size does not change considerably. The sintered part from the experiment has a relative density of 0.98, which is higher than our termination criteria of simulation, resulting in a much lower average pore size. However, the difference of pore size affected by the printing strategies has been captured by our experiment. A significantly higher pore size at the intermediate stage is obtained for the *0–0°* group and *0–90°* group and those larger pores cannot be fully eliminated in the sintered parts. At the final sintered stage, the average pore size from the *0–90°* group remains over 40 μm whereas the value is reduced to 27 μm for the *0–0°* group. The larger average pore size in the *0–90°* group indicates that the largest interconnected pores induced by the initial particle packing cannot be fully enclosed. The DEM simulation can be a good representation of the pore evolution trends, especially for the pore size distribution of the part undergoing different printing strategies.

In this study, the DEM tool is implemented to simulate the anisotropic sintering behavior of the part created by material extrusion AM. The method could directly enable different printing strategies embedded into the model and reveal their effects on microstructural evolution (grain morphology and pore evolution). For the anisotropic pore distribution, in particular, the DEM modeling can represent the location of pores as initiated by the printing strategy and then affected by the sintering process very well, offering an essential contribution to understanding the sintering phenomenon and predicting the final performance of the sintered part for industrial applications. Another advantage of the DEM methodology is that it does not require a significant number of computational resources compared with other approaches, such as the phase-field methodology. As an example, a domain for phase-field simulation can be discretized into millions of different cells with tens of millions of edges [49], whereas the DEM only requires tens of thousands of particles as individual elements to simulate the microstructure evolution. However, it is very important to ensure the convergence of macroscopic stress toward a correct value. The DEM simulation also requires a precise track of particle motion based on
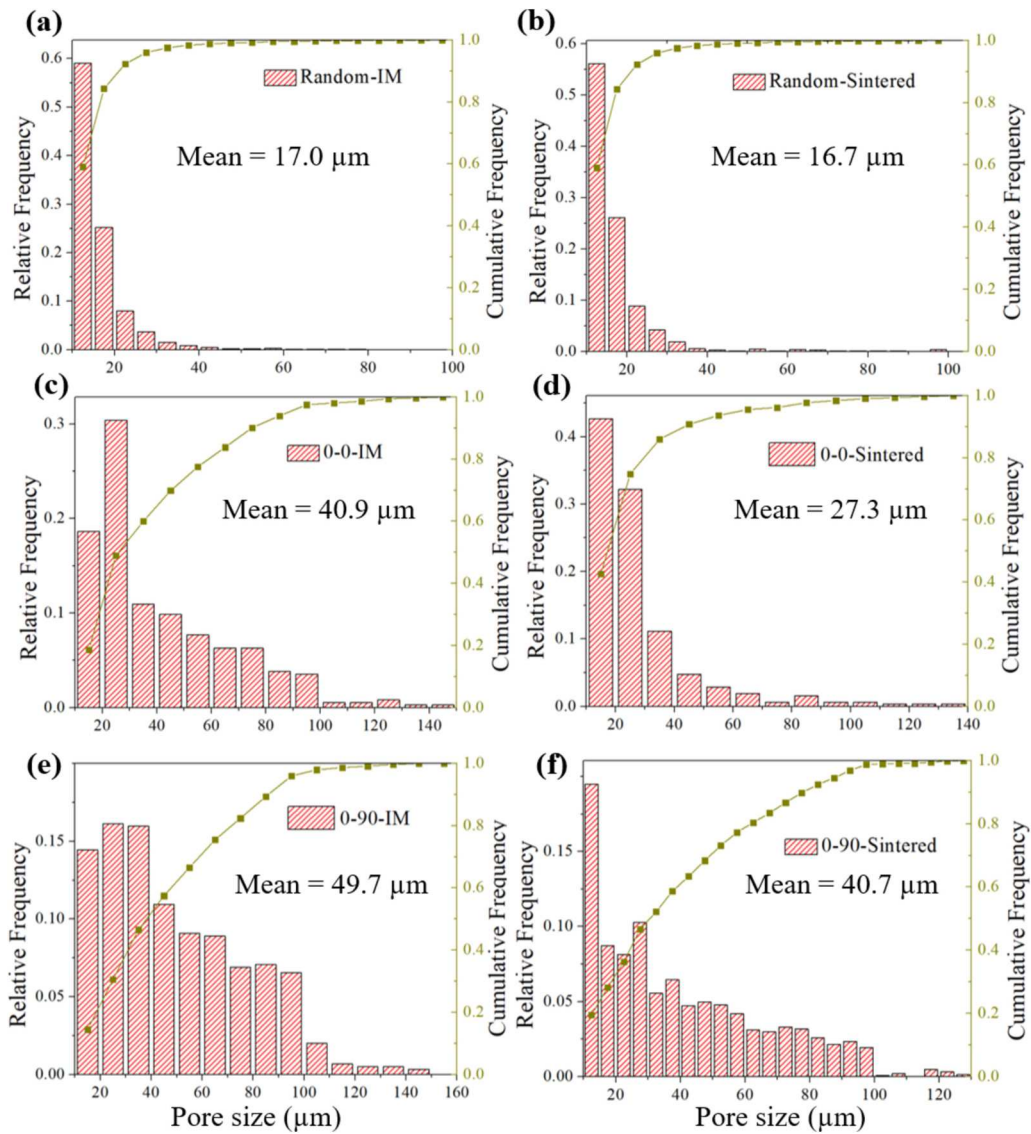
Fig. 12. Histograms of the pore size distribution of (a-b) Random group, (c-d) *0–0°*, and (e-f) *0–90°* group of specimens at two sintering stages from the X-ray CT data.

Newton's second law of motion, so the size of timestep is essential to the success of the simulation due to the tradeoff between model accuracy and computational cost. An extremely small timestep is usually given for a larger safety factor, sometimes unnecessarily increasing the computational time [50]. Overall, the DEM approach effectively solves the structural representation of large-packing of particles during sintering in a micro-length scale and its potential can be further realized in other AM-based approaches, e.g., binder jetting, selective laser sintering, etc. Future improvement of the DEM modeling could be enabled through the simulation of discrete elements in an irregular shape to represent polygonization of grain at later sintering stage. In addition, complex phenomena like phase transformation and grain polygonization can be embedded into the DEM models to reduce discrepancies in the predicted microstructure.

5. Conclusions

This study presents a fundamental investigation on the microstructure evolution during the extrusion-based sintering-assisted AM process via modeling, simulation, and experiments. Three initial large packing patterns of micro particles were employed, for the first time, to reveal

their effects on the pore evolution and grain growth during sintering process. X-ray CT scanning and microscopic observation were utilized to quantify the microstructure and validated the simulation results. The densification rate is the highest for the *Random* group compared to *0–0°* and *0–90°* packing, and the grain growth occurs at RD values over 0.8 for each group. The *0–0°* and *0–90°* packing strategies induce greater grain growth rate and result in higher final grain size compared with the *Random* group. Pores are concentrated at interlayer gaps at *0–0°* and *0–90°* groups and this distribution pattern has been captured by the X-ray CT imaging at both intermediate and final sintered stages. The number of pores is reduced from the intermediate sintering stage to the final sintering stage, but pores connect at later sintering stage to prevent further size reduction. The *0–90°* printing pattern creates the highest grain size and also the largest average pore size after sintering.

CRediT authorship contribution statement

Dayue Jiang: Writing – review & editing, Writing – original draft, Visualization, Validation, Software, Methodology, Data curation, Conceptualization. **Yue Zhou:** Validation, Software, Methodology, Data curation. **Mark D. Poliks:** Writing – review & editing, Supervision,

Resources, Methodology. **Peter Borgesen:** Writing – review & editing, Validation, Methodology, Conceptualization. **Fuda Ning:** Writing – review & editing, Supervision, Resources, Project administration, Methodology, Funding acquisition, Conceptualization.

Declaration of competing interest

The authors declare that they have no known competing financial interests or personal relationships that could have appeared to influence the work reported in this paper.

Appendix A. Binder-free "brown" part modeling procedure in dp3D

Particles, representing the fundamental element in the DEM code possess single crystallographic grain and will be packed together inside a simulation box. Each particle is regarded as a perfect sphere and labeled with a position in x, y, z coordinates and its radius. At the beginning of the packing process, a given number of particles will be randomly distributed inside the simulation box without any contact with each other. Those particles can be mono-sized or follow a given size distribution. This initial process produces a relative density of 0.3, where no contact is imposed to particles filled inside the simulation box. For the Random group, 12,500 particles are assigned into the box. For the other two packing patterns, 500 particles are assigned in a box with size ratio 1:5:1 and then the simulation boxes are stacked according to the illustration in Fig. 2. After that, a "jamming" process is introduced to the initial packing for a higher density. During the jamming process, a small value of macroscopic pressure (much less than the modulus of the particle material) is added on the boundary walls to reduce the volume of the simulation box. Thus, particles are "densified" by contacting with the neighbors, so the RD of particle system is increased. In this stage, only elastic interactions between particles will be activated. Specifically, the normal elastic contact force between two particles with radius R_1 and R_2 is given by the Hertzian law:

$$N^{Hertz} = \frac{4}{3} E^* R^{*1/2} \delta_n^{3/2} \tag{A1}$$

$$E^* = \left(\frac{1 - v_1^2}{E_1} + \frac{1 - v_2^2}{E_2} \right)^{-1} \tag{A2}$$

$$R^* = \left(\frac{1}{R_1} + \frac{1}{R_2} \right)^{-1} \tag{A3}$$

where N^{Hertz} is the normal contact force, r_1 and r_2, (E_1, v_1) and (E_2, v_2) represent the radii and elastic properties of those two particles, respectively, and δ_n is the normal indentation of the contact. The calculation of contact size follows the Hertz contact radius evolution eq. [20], which has been implemented in the dp3D code. After determination of the contact force, the particles are moved according to Newton's second law and their displacement is computed by a Velocity-Verlet algorithm [51]. The "jamming" process is terminated with a given relative density of 0.51 for the subsequent sintering simulation.

Data availability

The data that supports the findings of this study are available on request from the corresponding author, Fuda Ning.

References

[1] Gonzalez-Gutierrez J, Cano S, Schuschnigg S, Kukla C, Sapkota J, Holzer C. Additive manufacturing of metallic and ceramic components by the material extrusion of highly-filled polymers: a review and future perspectives. Mater 2018; 11. https://doi.org/10.3390/ma11050840.

[2] Thompson Y, Gonzalez-Gutierrez J, Kukla C, Felfer P. Fused filament fabrication, debinding and sintering as a low cost additive manufacturing method of 316L stainless steel. Addit Manuf 2019;30:100861. https://doi.org/10.1016/j.addma.2019.100861.

[3] Ding H, Zeng C, Raush J, Momeni K, Guo S. Developing fused deposition modeling additive manufacturing processing strategies for aluminum alloy 7075: sample preparation and metallographic characterization. Mater 2022;15. https://doi.org/10.3390/ma15041340.

[4] Liu B, Wang Y, Lin Z, Zhang T. Creating metal parts by fused deposition modeling and sintering. Mater Lett 2020;263:127252. https://doi.org/10.1016/j.matlet.2019.127252.

[5] Kurose T, Abe Y, Santos MVA, Kanaya Y, Ishigami A, Tanaka S, et al. Influence of the layer directions on the properties of 316L stainless steel parts fabricated through fused deposition of metals. Mater 2020;13. https://doi.org/10.3390/ma13112493.

[6] Pellegrini A, Guerra MG, Lavecchia F. Shrinkage evaluation and geometric accuracy assessment on 17–4 PH samples made by material extrusion additive manufacturing. J Manuf Process 2024;109:394–406. https://doi.org/10.1016/j.jmapro.2023.12.031.

[7] Li S, Deng H, Lan X, He B, Li X, Wang Z. Developing cost-effective indirect manufacturing of H13 steel from extrusion-printing to post-processing. Addit Manuf 2023;62:103384. https://doi.org/10.1016/j.addma.2022.103384.

[8] Zhang Y, Zhang J. Sintering phenomena and mechanical strength of nickel based materials in direct metal laser sintering process—a molecular dynamics study. J Mater Res 2016;31:2233–43. https://doi.org/10.1557/jmr.2016.230.

[9] Ding L, Davidchack RL, Pan J. A molecular dynamics study of sintering between nanoparticles. Comput Mater Sci 2009;45:247–56. https://doi.org/10.1016/j.commatsci.2008.09.021.

[10] Bordia RK, Kang S-JL, Olevsky EA. Current understanding and future research directions at the onset of the next century of sintering science and technology. J Am Ceram Soc 2017;100:2314–52. https://doi.org/10.1111/jace.14919.

[11] Zhang Y, Xiao X, Zhang J. Kinetic Monte Carlo simulation of sintering behavior of additively manufactured stainless steel powder particles using reconstructed microstructures from synchrotron X-ray microtomography. Results Phys 2019;13: 102336. https://doi.org/10.1016/j.rinp.2019.102336.

[12] Tikare V, Braginsky M, Bouvard D, Vagnon A. Numerical simulation of microstructural evolution during sintering at the mesoscale in a 3D powder compact. Comput Mater Sci 2010;48:317–25. https://doi.org/10.1016/j.commatsci.2010.01.013.

[13] Hara S, Ohi A, Shikazono N. Sintering analysis of sub-micron-sized nickel powders: kinetic Monte Carlo simulation verified by FIB–SEM reconstruction. J Power Sources 2015;276:105–12. https://doi.org/10.1016/j.jpowsour.2014.11.110.

[14] Asp K, Ågren J. Phase-field simulation of sintering and related phenomena – a vacancy diffusion approach. Acta Mater 2006;54:1241–8. https://doi.org/10.1016/j.actamat.2005.11.005.

[15] Wang YU. Computer modeling and simulation of solid-state sintering: a phase field approach. Acta Mater 2006;54:953–61. https://doi.org/10.1016/j.actamat.2005.10.032.

[16] Martin CL, Schneider LCR, Olmos L, Bouvard D. Discrete element modeling of metallic powder sintering. Scr Mater 2006;55:425–8. https://doi.org/10.1016/j.scriptamat.2006.05.017.

[17] Olevsky EA, Tikare V, Garino T. Multi-scale study of sintering: a review. J Am Ceram Soc 2006;89:1914–22. https://doi.org/10.1111/j.1551-2916.2006.01054.x.

[18] Martin CL, Yan Z, Jauffres D, Bouvard D, Bordia RK. Sintered ceramics with controlled microstructures: numerical investigations with the Discrete Element Method. J Ceram Soc Japan 2016;124:340–5. https://doi.org/10.2109/jcersj2.15269.

[19] Parhami F, McMeeking RM. A network model for initial stage sintering. Mech Mater 1998;27:111–24. https://doi.org/10.1016/S0167-6636(97)00034-3.

[20] Coble RL. Initial sintering of alumina and hematite. J Am Ceram Soc 1958;41:55–62. https://doi.org/10.1111/j.1151-2916.1958.tb13519.x.

[21] Pan J, Le H, Kucherenko S, Yeomans JA. A model for the sintering of spherical particles of different sizes by solid state diffusion. Acta Mater 1998;46:4671–90. https://doi.org/10.1016/S1359-6454(98)00144-X.

[22] Henrich B, Wonisch A, Kraft T, Moseler M, Riedel H. Simulations of the influence of rearrangement during sintering. Acta Mater 2007;55:753–62. https://doi.org/10.1016/j.actamat.2006.09.005.

[23] Martin S, Guessasma M, Léchelle J, Fortin J, Saleh K, Adenot F. Simulation of sintering using a Non Smooth Discrete Element Method. Application to the study of rearrangement. Comput Mater Sci 2014;84:31–9. https://doi.org/10.1016/j.commatsci.2013.11.050.

[24] Olmos L, Martin CL, Bouvard D. Sintering of mixtures of powders: experiments and modelling. Powder Technol 2009;190:134–40. https://doi.org/10.1016/j.powtec.2008.04.057.

[25] Olevsky EA. Theory of sintering: from discrete to continuum. Mater Sci Eng R Rep 1998;23:41–100. https://doi.org/10.1016/S0927-796X(98)00009-6.

[26] Martin CL, Camacho-Montes H, Olmos L, Bouvard D, Bordia RK. Evolution of defects during sintering: discrete element simulations. J Am Ceram Soc 2009;92:1435–41. https://doi.org/10.1111/j.1551-2916.2009.03014.x.

[27] Paredes-Goyes B, Jauffres D, Missiaen JM, Martin CL. Grain growth in sintering: a discrete element model on large packings. Acta Mater 2021;218:117182. https://doi.org/10.1016/j.actamat.2021.117182.

[28] Hugonnet B, Missiaen J-M, Martin CL, Rado C. Effect of contact alignment on shrinkage anisotropy during sintering: stereological model, discrete element model and experiments on NdFeB compacts. Mater Des 2020;191:108575. https://doi.org/10.1016/j.matdes.2020.108575.

[29] User guide for dp3D. https://www.overleaf.com/project/61370d663a049547c72bcf36.

[30] Shrestha R, Simsiriwong J, Shamsaei N. Fatigue behavior of additive manufactured 316L stainless steel parts: effects of layer orientation and surface roughness. Addit Manuf 2019;28:23–38. https://doi.org/10.1016/j.addma.2019.04.011.

[31] Jiang D, Ning F. Anisotropic deformation of 316L stainless steel overhang structures built by material extrusion based additive manufacturing. Addit Manuf 2022;50:102545. https://doi.org/10.1016/j.addma.2021.102545.

[32] Kumar R, Rommel S, Jauffrès D, Lhuissier P, Martin CL. Effect of packing characteristics on the discrete element simulation of elasticity and buckling. Int J Mech Sci 2016;110:14–21. https://doi.org/10.1016/j.ijmecsci.2016.02.009.

[33] Hamelin J, Jauffrés D, Martin CL, Meille S, Foray G. Mechanical properties of milimetric silica aerogel particles produced through evaporative drying: a coupled experimental and discrete element approach. J Non Cryst Solids 2021;560:120727. https://doi.org/10.1016/j.jnoncrysol.2021.120727.

[34] Radi K, Jauffrès D, Deville S, Martin CL. Elasticity and fracture of brick and mortar materials using discrete element simulations. J Mech Phys Solids 2019;126:101–16. https://doi.org/10.1016/j.jmps.2019.02.009.

[35] Nogueira G, Gervais T, Peres V, Marc E, Martin CL. Using discrete simulations of compaction and sintering to predict final part geometry. Powder Metall 2023;66:208–15. https://doi.org/10.1080/00325899.2023.2198796.

[36] Murch GE. Ferrite and austenite: diffusion, bulk and interfacial. Encycl Mater Sci Technol 2001:3009–12. https://doi.org/10.1016/b0-08-043152-6/00536-2.

[37] Johnson DL. New method of obtaining volume, grain-boundary, and surface diffusion coefficients from sintering data. J Appl Phys 2003;40:192–200. https://doi.org/10.1063/1.1657030.

[38] Maalekian M, Radis R, Militzer M, Moreau A, Poole WJ. In situ measurement and modelling of austenite grain growth in a Ti/Nb microalloyed steel. Acta Mater 2012;60:1015–26. https://doi.org/10.1016/j.actamat.2011.11.016.

[39] Wang Z, Li H, Shen Q, Liu W, Wang Z. Nano-precipitates evolution and their effects on mechanical properties of 17-4 precipitation-hardening stainless steel. Acta Mater 2018;156:158–71. https://doi.org/10.1016/j.actamat.2018.06.031.

[40] ISO 643:2019. Steels – micrographic determination of the apparent grain size. https://www.iso.org/obp/ui/#iso:std:iso:643:ed-4:v2:en.

[41] You S, Jiang D, Wang F, Ning F. Anisotropic sintering shrinkage behavior of stainless steel fabricated by extrusion-based metal additive manufacturing. J Manuf Process 2023;101:1508–20. https://doi.org/10.1016/j.jmapro.2023.07.026.

[42] Kerbart G, Manière C, Harnois C, Marinel S. Predicting final stage sintering grain growth affected by porosity. Appl Mater Today 2020;20:100759. https://doi.org/10.1016/j.apmt.2020.100759.

[43] German RM. Coarsening in sintering: grain shape distribution, grain size distribution, and grain growth kinetics in solid-pore systems. Crit Rev Solid State Mater Sci 2010;35:263–305. https://doi.org/10.1080/10408436.2010.525197.

[44] Huber D, Vogel L, Fischer A. The effects of sintering temperature and hold time on densification, mechanical properties and microstructural characteristics of binder jet 3D printed 17-4 PH stainless steel. Addit Manuf 2021;46:102114. https://doi.org/10.1016/j.addma.2021.102114.

[45] Henry TC, Morales MA, Cole DP, Shumeyko CM, Riddick JC. Mechanical behavior of 17-4 PH stainless steel processed by atomic diffusion additive manufacturing. Int J Adv Manuf Technol 2021;114:2103–14. https://doi.org/10.1007/s00170-021-06785-1.

[46] German RM. Sintering trajectories: description on how density, surface area, and grain size change. JOM 2016;68:878–84. https://doi.org/10.1007/s11837-015-1795-8.

[47] Quintana-Ruiz OD, Campello EMB. Discrete element modeling of selective laser sintering additive manufacturing processes. Comput Methods Appl Mech Eng 2023;410:115994. https://doi.org/10.1016/j.cma.2023.115994.

[48] Zhu Y, Wu Z, Hartley WD, Sietins JM, Williams CB, Yu HZ. Unraveling pore evolution in post-processing of binder jetting materials: X-ray computed tomography, computer vision, and machine learning. Addit Manuf 2020;34:101183. https://doi.org/10.1016/j.addma.2020.101183.

[49] Yang M, Wang L, Yan W. Phase-field modeling of grain evolutions in additive manufacturing from nucleation, growth, to coarsening. Npj Comput Mater 2021;7:56. https://doi.org/10.1038/s41524-021-00524-6.

[50] Burns SJ, Piiroinen PT, Hanley KJ. Critical time step for DEM simulations of dynamic systems using a Hertzian contact model. Int J Numer Methods Eng 2019;119:432–51. https://doi.org/10.1002/nme.6056.

[51] Delacroix B, Bouarab A, Fradette L, Bertrand F, Blais B. Simulation of granular flow in a rotating frame of reference using the discrete element method. Powder Technol 2020;369:146–61. https://doi.org/10.1016/j.powtec.2020.05.006.